

X-ray polarimetric features of Gamma-ray Bursts across varied redshifts and hints for Axion-Like-Particles

Qingxiang Zhang¹, Feng Huang^{1,*}, Zhongxiang Wang², Taotao Fang¹

¹*Department of Astronomy, Xiamen University, Xiamen, Fujian 361005, China*

²*Department of Astronomy, School of Physics and Astronomy, Yunnan University, Kunming 650091, China*

(Dated: April 12, 2024)

Polarimetric features during the prompt phase of Gamma-ray Bursts (GRBs) have been essential for elucidating the debated emission mechanisms and gaining insight into the inner structure of GRBs. However, the potential impact of photon-Axion-Like-Particle (ALP) mixing in extragalactic magnetic fields, leading to significant modifications to the initial polarization state, has been overlooked in discussions concerning prompt phase constraints. In this work, we first examine the statistical characteristics of linear polarization degree (Π_L) in GRBs, by utilizing data from polarimetric missions focusing on sub-MeV emissions. Our analysis, conducted with a restricted sample of GRBs spanning various redshifts, reveals a diverse distribution of Π_L , which currently shows no correlation with the GRBs' spectral parameters or properties of candidate host galaxies. We then explore alternations to the initial Π_L due to photon-ALP mixing within a domain-like structure of the intergalactic magnetic field (\mathbf{B}_{IGM}), considering various parameter sets associated with ALPs and \mathbf{B}_{IGM} . With the existence of ALPs with mass $m_a \lesssim 10^{-14}$ eV and photon-ALP coupling constant $g_{a\gamma} \simeq 0.5 \times 10^{-11}$ GeV⁻¹, we find that fully linearly polarized photons ($\Pi_{L_0} = 1$) may experience a polarization reduction of up to 20%, whereas for unpolarized photons ($\Pi_{L_0} = 0$), the mixing can increase polarization by up to 40% for GRBs with redshifts above approximately 1. To ensure that the effect of mixing is small enough to be negligible, the mixing term $\Delta_{a\gamma} \equiv 1/2 g_{a\gamma} \mathbf{B}_{\text{IGM}}$ should be less than 1.5×10^{-4} Mpc⁻¹. Currently, the number of GRBs with both sub-MeV polarization measurement and redshift confirmation remains very limited. Half of the GRBs with available polarization data have Π_L being less than 30%. Certification of redshift for this subset of GRBs would further constrain the parameter space of low-mass ALPs or provide an independent means to determine the upper limit on \mathbf{B}_{IGM} .

I. INTRODUCTION

GRBs are among the most energetic events observed in the universe and their prompt phase is characterized by a sudden and intense release of gamma-rays with energies spanning from tens of keV to several MeV. Despite considerable advancements in observation and theory, elucidating the origin of this emission remains a complex challenge due to the diverse nature and intricate physics involved. Ongoing research aims to decipher spectral features and temporal evolution across various emission mechanisms and geometric structures [1]. While spectral data alone prove insufficient, polarimetric measurements are crucial in clarifying the prompt-emission nature and inner structure of GRBs. However, it is important to recognize that the measured value of polarization is typically ascribed to photons emitted by GRBs, hardly considering possible propagation effects in extragalactic space. Such effects could appreciably affect both the flux and polarization state of high-energy photons originating from distant energetic sources, particularly in models incorporating the existence of ALPs, which are very light spin-zero particles predicted by numerous extensions of the Standard Model [2].

Recently, ALPs have been increasingly highlighted as promising candidates for dark matter. ALPs are re-

garded as generalized forms of axions, exhibiting less stringent correlations between its mass and coupling constant compared to axions. Observations of high-energy astrophysical sources have sparked significant interest in narrowing down the parameter space of ALPs and seeking evidence of their existence. The recent observability of very-high-energy emission (above 10 TeV, [3]) from GRB 221009A, known as the Brightest Of All Time (BOAT), has been considered a potential indication of ALP existence [4]. This observation offers a possible explanation for the significant decrease in the optical depth of TeV photons, attributed to photon-ALP mixing in external magnetic fields, a key characteristic of ALPs as described by the Lagrangian term

$$\mathcal{L}_{a\gamma} = g_{a\gamma} \mathbf{E} \cdot \mathbf{B} a, \quad (1)$$

where $g_{a\gamma}$ is the coupling constant of the photon-ALP mixing, \mathbf{E} and \mathbf{B} refer to the electric and magnetic fields respectively.

Similar to this scenario of photon-ALP mixing, previous investigations concerning anomalies in the transparency of the universe have primarily centered on analyzing the spectral characteristics of TeV photons emitted from cosmological sources [5–11]. Furthermore, potential spectral deviations in GeV emissions from blazars have been attributed to photon-ALP mixing in various magnetic fields, including those within jets, intracluster environments, intergalactic space, and the Milky Way [12–18]. Corresponding constraints on the photon-ALP coupling constant $g_{a\gamma}$ have been derived for the mass of

*Corresponding author: fenghuang@xmu.edu.cn

ALPs (m_a) ranging from 10^{-10} eV to 10^{-7} eV. For a recent comprehensive review of these constraints, refer to Ref. [19] and references therein.

In addition to case studies examining the effects of photon-ALP mixing, larger samples at cosmological distances could offer a statistical perspective on this issue. The scatter in the luminosity relations of a substantial sample of active galactic nuclei (AGN) has been utilized to search for ALPs [20]. Ref. [21] identified a correlation between spectral slope and redshift in the observed γ -ray spectra of blazars, assuming a consistent intrinsic emission spectrum for sources at different redshifts, and this phenomenon has been effectively explained in Ref. [22] through the scenario of photon-ALP mixing in intergalactic magnetic fields for blazars with redshifts up to 0.6. A more recent study has further investigated this correlation with a sample of blazars with redshift up to 1, confirming the necessity of photon-ALP mixing to explain the correlation within the redshift range of 0.2 to 1 [23].

Due to the spin-zero nature of ALPs, their mixing with photons in external magnetic fields not only affects the flux of photons but also alters their polarization states. The early spike in interest examining the effects of this mixing on the polarization state of photons stemmed from the reasonable explanation for observations of polarization in quasars at optical wavelengths. The observed large-scale alignment of quasar polarizations at different redshifts [24–27] and optical circular polarization observed in several quasars have been considered as hints for the existence of ALPs [27]. More recently, based on the absence of detectable optical circular polarization from blazars at a level of 0.1%, Ref. [28] have placed constraints on the ALPs-photon mixing term, limiting it to $g_{a\gamma} \cdot \mathbf{B}_{\text{jet}} \lesssim 7.9 \times 10^{-12} \text{ G} \cdot \text{GeV}^{-1}$ for axion masses $m_a \lesssim 10^{-13}$ eV (\mathbf{B}_{jet} refers to the magnetic field in the jet of blazar). For even low-energy photons, the mixing of ALPs with cosmic microwave background (CMB) photons has tended to influence the intensity of the CMB, as well as its linear and circular polarization, leading to distortions of the CMB spectrum, which subsequently imposed strong constraints on ALP parameters with the latest observations from CMB [29, 30]. For higher-energy photons, theoretical exploration of the propagation of X-ray to γ ray photons originating from the central region of a cluster of galaxies or within the jet of a blazar has been undertaken in a series of articles [31–34]. An expected feature related to our purpose is that unpolarized photons from the source at a cosmological distance become partially polarized due to the photon-ALP mixing, possibly resulting in measurable modifications to the initial Π_L .

The concept of utilizing polarized prompt emission from GRBs to constrain ALP parameters has been investigated in several studies. In Ref. [35], photon-ALP mixing was hypothesized to occur in the inner jet region, with empirical investigations placing constraints on $g_{a\gamma} \lesssim 10^{-12} \text{ GeV}^{-1}$ for ALPs with $m_a = 10^{-3}$ eV. An-

other study focused on photon mixing in the internal shocks region of GRBs with a magnetic field strength of 10^6 G, revealing alterations in both the early-time evolution pattern of Π_L and the spectral shape compared to synchrotron radiation models [36]. Additionally, a comprehensive examination of the modification of photon polarization emitted from GRBs due to extragalactic magnetic fields was conducted, demonstrating that the existence of ALPs could contribute to broadening the polarization distribution of photons [37]. Similar conclusions were drawn in Ref. [38], where two different configurations of the intergalactic magnetic field (IGM) \mathbf{B}_{IGM} were considered. Their analytical and numerical calculations indicated that Π_L tends towards an asymptotic value as the distance increases, which remains independent of the assumed magnetic field configuration.

The above earlier research primarily focused on the impact of photon-ALP mixing from the theoretical phenomenological model discussions, given the lack of polarimetric detection techniques at higher energies. However, this situation has changed in the past decades, particularly within the sub-MeV energy range. Early-stage space-borne X-ray polarimeters, such as IPS (100 keV–1 MeV) and IBIS (15 keV–10 MeV) on the INTEGRAL satellite, have contributed to the advancement [39]. Moreover, the first two dedicated GRB polarimeters, namely the Gamma-Ray Burst Polarimeter (GAP, 70–300 keV) [40] and POLAR (50–500 keV) [41], have recorded numerous detections of GRB polarization. The AstroSAT satellite is presently operational with a polarimeter (CZTI) covering energies from 100 keV to 600 keV [42], and it has also released a relatively large catalog of GRBs with polarization measurements. In this article, we will start with analyzing the statistical characteristics of Π_L released by these X-ray polarimetric missions, and investigate modifications to the initial Π_L resulting primarily from photon-ALP mixing within a domain-like structure of the intergalactic magnetic field, following the main framework of Ref. [37].

The paper is organized as follows. In Sec. II, we analyze the statistical properties of Π_L data obtained by X-ray polarimetric missions. In Sec. III, we delve into the fundamental framework of photon-ALP mixing in external magnetic fields. In Sec. IV, we present results related to modifications of the initial linear polarization degree Π_L observed in GRBs, considering a range of ALP and magnetic field parameters. Finally, Sec. V encompasses the conclusions and discussions.

II. STATISTICAL CHARACTERISTICS OF Π_L

A. Π_L Distribution

GRBs' Π_L distribution. To begin with, we conducted a thorough investigation of GRBs with available polarimetric observations. Based on the recently released catalogs of POLAR and AstroSAT and early observations

| GRB | Π_L (%) | α_s | β_s | E_p (keV) | Fluence (10^{-6} erg cm^{-2}) | Instrument | Redshift* | Offset |
|------------|---------------------------|-------------------------|-------------------------|----------------------|--|-------------------------|--------------------------------|------------------|
| 1 200311A | < 45.41 | $-0.95^{+0.02}_{-0.02}$ | $-2.57^{+0.19}_{-0.19}$ | 1218^{+110}_{-110} | $42.543^{+0.12789}_{-0.12789}$ | AstroSAT ^I | $0.0838^{+0.0349^a}_{-0.0302}$ | 0.072'/8.00kpc |
| 2 180103A | $71.43^{+26.84}_{-26.84}$ | $-1.31^{+0.06}_{-0.06}$ | $-2.24^{+0.90}_{-0.13}$ | 273^{+26}_{-23} | 223 | AstroSAT ^I | $0.037^{+0.0063^a}_{-0.0015}$ | 0.184'/8.75kpc |
| 3 180427A | $60.01^{+22.32}_{-22.32}$ | $-0.29^{+0.08}_{-0.08}$ | $-2.80^{+0.16}_{-0.16}$ | 147^{+2}_{-2} | $50.455^{+0.12559}_{-0.12559}$ | AstroSAT ^I | $0.0309^{+0.045^a}_{-0.0309}$ | 0.273'/10.81kpc |
| 4 200412A | < 53.84 | $-0.70^{+0.05}_{-0.05}$ | $-2.50^{+0.21}_{-0.21}$ | 256^{+8}_{-7} | $28.750^{+0.097405}_{-0.097405}$ | AstroSAT ^I | $0.1055^{+0.0192^a}_{-0.0145}$ | 0.131'/18.74kpc |
| 5 061122A | 11^{+48}_{-11} | $-1.14^{+0.27}_{-0.32}$ | $-1.91^{+0.07}_{-0.10}$ | 70^{+106}_{-63} | 20 | INTEGRAL ^{II} | $1.33^{+0.77^b}_{-0.76}$ | 0.435''/20.13kpc |
| 6 200806A | < 54.73 | -0.53 | -2.96 | 109.12 | 1 | AstroSAT ^I | $0.1148^{+0.1749^a}_{-0.1148}$ | 0.234'/36.58kpc |
| 7 190530A | $46.85^{+18.53}_{-18.53}$ | $-0.99^{+0.02}_{-0.00}$ | $-3.50^{+0.25}_{-0.25}$ | 888^{+8}_{-8} | $370.62^{+0.052475}_{-0.052475}$ | AstroSAT ^I | 0.9386 ^c | - |
| 8 180914B | $48.48^{+19.69}_{-19.69}$ | $-0.75^{+0.04}_{-0.04}$ | $-2.10^{+0.08}_{-0.70}$ | 453^{+26}_{-24} | 598 | AstroSAT ^I | 1.096 ^d | - |
| 9 171010A | < 30.02 | $-1.12^{+0.01}_{-0.00}$ | $-2.39^{+0.02}_{-0.02}$ | 180^{+3}_{-3} | $632.79^{+0.098525}_{-0.098525}$ | AstroSAT ^I | 0.3285 ^d | - |
| 10 160703A | < 62.64 | $-0.78^{+0.12}_{-0.09}$ | < -2.48 | 351^{+40}_{-46} | 9 | AstroSAT ^I | < 1.5 ^d | - |
| 11 160623A | < 56.51 | $-0.94^{+0.02}_{-0.02}$ | $-2.83^{+0.09}_{-0.10}$ | 662^{+19}_{-18} | $3.9564^{+0.068702}_{-0.068702}$ | AstroSAT ^I | 0.367 ^d | - |
| 12 160509A | < 92 | $-0.75^{+0.02}_{-0.02}$ | $-2.13^{+0.03}_{-0.03}$ | 334^{+12}_{-10} | $178.98^{+0.14957}_{-0.14957}$ | AstroSAT ^{III} | 1.17 ^d | - |
| 13 160131A | 94^{+33}_{-33} | $-1.16^{+0.04}_{-0.04}$ | $-1.56^{+0.07}_{-0.10}$ | 586^{+518}_{-259} | 20.4 | AstroSAT ^{III} | 0.972 ^d | - |
| 14 140206A | > 48 | $-0.94^{+0.08}_{-0.08}$ | $-2.0^{+0.20}_{-0.30}$ | 98^{+17}_{-17} | $15.520^{+0.074778}_{-0.074778}$ | INTEGRAL ^{IV} | $2.739^{+0.001^e}_{-0.001}$ | - |

TABLE I: The list of the 14 GRBs we collected with Π_L and redshifts.

I: Ref. [42], II: Ref. [43], III: Ref. [44], IV: Ref. [45].

*: 1–6 is the photometric redshift of host galaxy; 7–9, 11–14 is spectral redshift; 10 is the upper limit of redshift.

a: The results obtained from calculations based on photometry data, b: Ref. [46], c: Ref. [47], d: <https://www.mpe.mpg.de/~jcg/grbgen.html> e: Ref. [45].

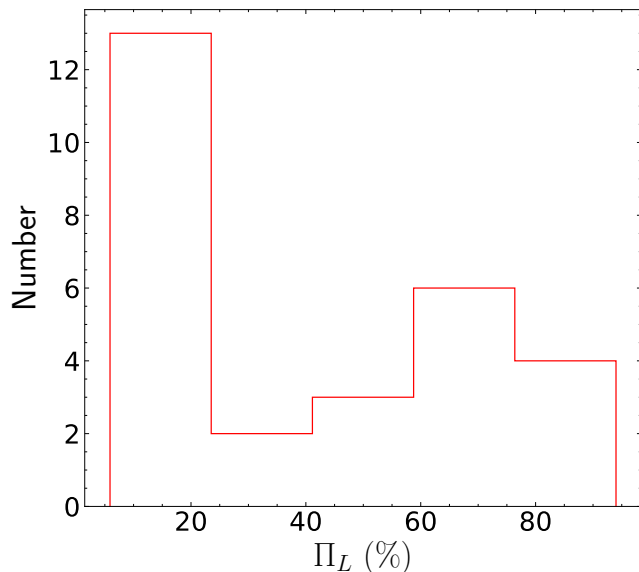


FIG. 1: Histogram of Π_L for 28 sources with the detected value.

of INTEGRAL etc. [41, 42, 44], we have obtained a sample with 50 GRBs observed by polarimeters in the sub-MeV band. Some of these sources have also been studied individually [43, 45], and several of them are found in the lists of Ref. [48] and Ref. [49]. GRB221009A, the

BOAT, has been observed by IXPE, the newly launched polarimeter in the soft X-ray band [50]. We have ignored this detection for its meager relevance to the prompt phase. The value of GRB061122A's Π_L is controversial. The results obtained from Ref. [43] and Ref. [46] are almost incompatible. For it, we used the polarization obtained in Ref. [43] in the 100–350 keV range. Among the 50 GRBs, there are 28 sources with polarization measurements, 19 with upper limits, and 3 with lower limits. The histogram of Π_L is shown in Fig. 1. Among the 28 measurements, 12 exhibited Π_L values below 20%, while 4 sources had Π_L values above 80%.

Numerical simulations have been conducted in optically thin synchrotron models [51] or photospheric models with dissipation [52], which are the two most popular models used to explain the origin of prompt radiation. Ref. [51] investigated the statistical properties of the polarization of GRBs using Monte Carlo simulations, assuming three different jet structures. They discovered that approximately one-third of GRBs exhibit Π_L values clustered between 20% and 70%, stemming from synchrotron emission within a globally ordered magnetic field. If several GRBs with $\Pi_L > 80\%$ are observed, then the Compton Drag model will be favored. In Ref. [52], it is predicted that $\Pi_L < 4\%$ from the jet core and tends to increase with viewing angle outside of the core, reaching levels as high as 20%–40% in photospheric models with dissipation. As shown in Fig. 1, the majority of Π_L values are less than 70%, with sub-samples clustering below 20%

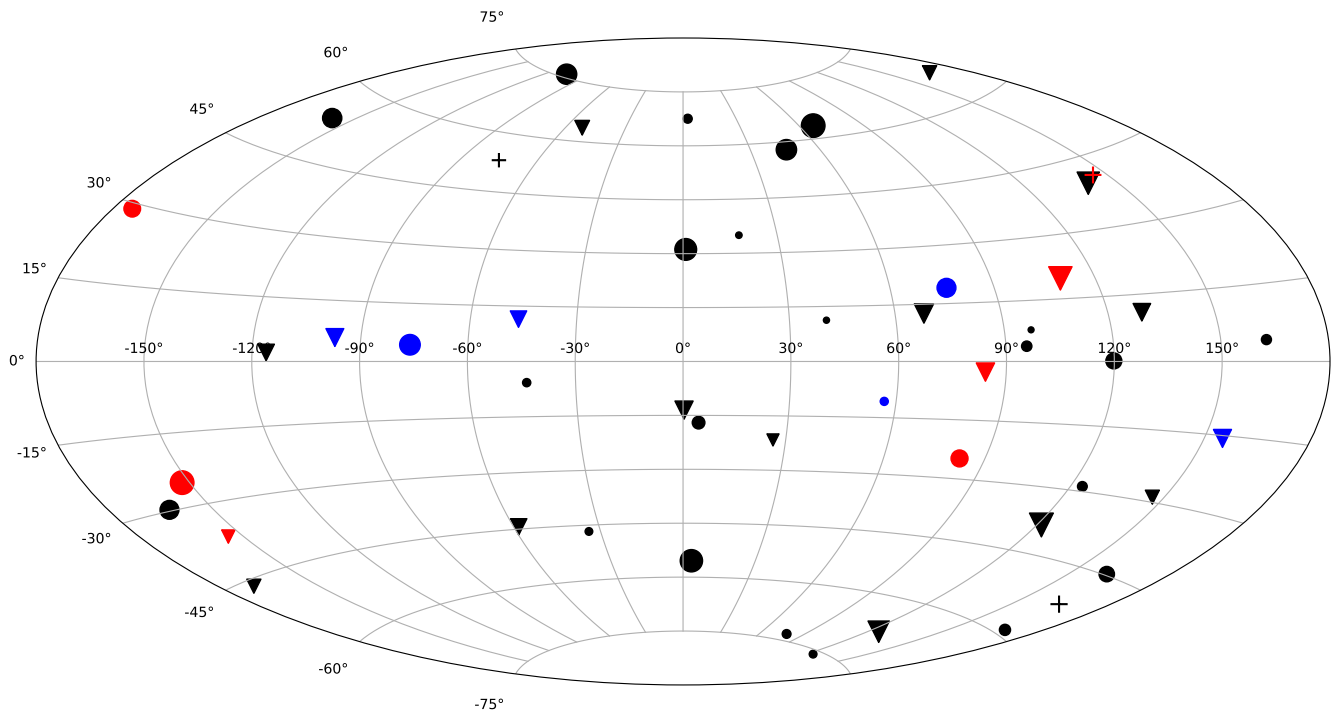


FIG. 2: All-sky distribution of 50 GRBs in Galactic coordinates. Dots indicate sources with measured Π_L . Inverted triangles represent sources with upper limits on Π_L , and plus signs represent lower limits. The red/blue data points represent sources with spectroscopic/photometric redshifts. Symbol size reflects the relative magnitude of Π_L .

and several cases exceeding 80%. Given the current observed number and distribution of Π_L , the controversies persist, and distinguishing between these models remains challenging.

GRBs’ spatial distribution. The distribution of these 50 GRBs in the sky in Galactic coordinates is shown in Fig. 2. The dots represent GRBs with observed values of Π_L . The inverted triangles represent GRBs with upper limits while the plus signs represent GRBs with lower limits. The red/blue color indicates GRBs with spectroscopic/photometric redshifts (redshift recognition will be presented in the following paragraph). The relative sizes of the symbols in the figure represent the relative magnitudes of values of Π_L . Despite the limited sample size, the GRBs show no apparent clustering in the sky.

GRBs’ redshifts. The presence of ALPs has the potential to alter the initial linear polarization degree of GRB prompt emission. However, the extent of this modification heavily relies on the distance traveled by the GRB within a domain-like structure of \mathbf{B}_{IGM} . Accurate redshift determination is crucial in this context. Hence, we conducted a cross-matching analysis between our sample and the publicly available catalog¹, which

provides a subjective collection of the localization of GRBs. Through this analysis, we identified a total of 8 sources that exhibited an overlap. The corresponding sources are displayed in Table I, with the redshift values denoted as superscripts ‘c’, ‘d’ or ‘e’. Among these, 7 sources have spectroscopic redshifts, while one has a spectroscopic redshift upper limit. Regarding the source GRB 190530A, initially available with a spectroscopic redshift upper limit, we acquired its precise spectroscopic redshift from Ref. [47]. For GRB 061122A, we utilized the photometric redshift of its candidate host galaxy in Ref. [46]. For sources lacking documented redshift information, we conducted a search for their candidate host galaxies in the NASA/IPAC Extragalactic Database (NED)² within an angular separation of $30''$. We assumed that the redshift of a GRB equals that of its candidate host galaxy. Utilizing the photometric data of these candidate host galaxies, we calculated their photometric redshifts using Le PHARE³. Sources lacking sufficient photometric data or exhibiting large fitting errors or significant χ^2 values were excluded from our sample. Additionally, we calculated the offset between the candidate host galaxy and the GRB localization, excluding

¹ <https://www.mpe.mpg.de/~jcg/grbgen.html>

² <https://ned.ipac.caltech.edu/>

³ <https://www.cfht.hawaii.edu/~arnouts/LEPHARE/lephare.html>

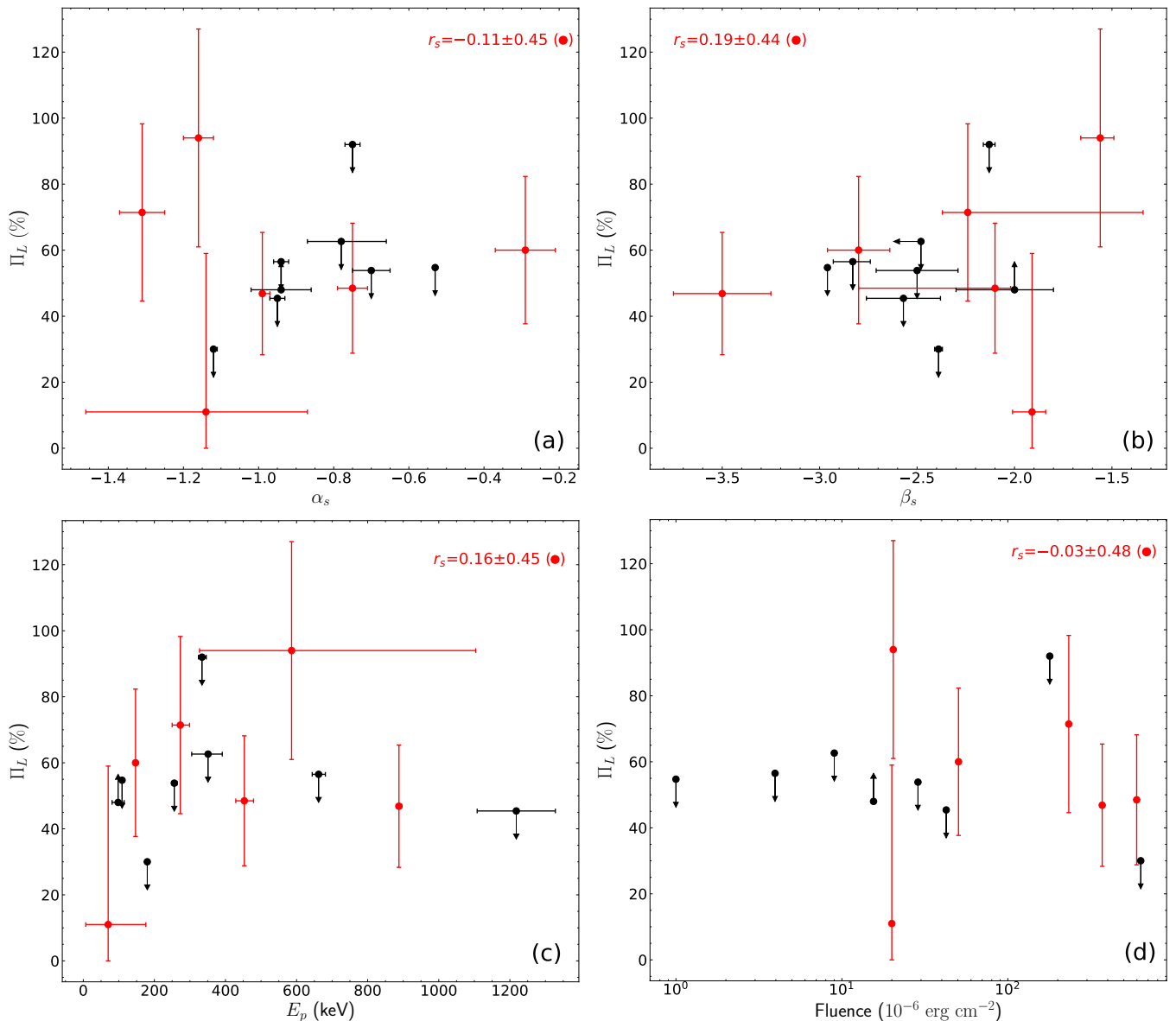


FIG. 3: Comparison between Π_L and the spectral parameters of the GRBs. The red color denotes sources with measured Π_L whereas black represents sources with Π_L constrained as an upper limit or lower limit. (a) Π_L vs. α_s with $r_s = -0.11 \pm 0.45$. (b) Π_L vs. β_s with $r_s = 0.19 \pm 0.44$. (c) Π_L vs. E_p with $r_s = 0.16 \pm 0.45$. (d) Π_L vs. Fluence with $r_s = -0.03 \pm 0.48$. r_s values are exclusively derived from the red dots.

sources with large offsets. This resulted in 5 GRBs with candidate host galaxies (Table I). Our final dataset comprised 14 sources. For a detailed listing of them, along with Π_L and redshift, refer to Table I.

The measured Π_L s of GRBs span a large range, while the mechanisms responsible for the diversity remain inadequately explored. Previous research generally suggests that the inner structure of the GRB itself interacts with the host galaxy, potentially influencing this variability. However, the surrounding environment of GRBs and the internal dynamics of the jets are complex and not fully understood, making it challenging to accurately model the emission process. In the subsequent two subsections,

we will explore the potential relationships between Π_L and the spectral characteristics of GRB's prompt emission, as well as those between Π_L and the properties of GRBs' host galaxies.

B. Π_L vs. Spectral Parameters

The intense bursts of high-energy gamma rays from GRBs are commonly detected by instruments such as Swift/BAT and Fermi/GBM. The observed nonthermal features of these spectra are typically utilized to distinguish between optical thin synchrotron models [51] or

| GRB | Π_L (%) | M_\star ($10^8 M_\odot$) | M_{gas} ($10^8 M_\odot$) | SFR ($M_\odot \text{ yr}^{-1}$) | sSFR (Gyr^{-1}) | Instrument | Redshift* | Offset |
|-----------|---------------------------|---------------------------------|-------------------------------------|-----------------------------------|----------------------------|------------------------|--------------------------------|-----------------|
| 1 200311A | < 45.41 | $138.10^{+114.39}_{-114.39}$ | $48.05^{+51.67}_{-51.67}$ | $17.56^{+16.72}_{-16.72}$ | $1.27^{+1.60}_{-1.60}$ | AstroSAT ^I | $0.0838^{+0.0349^a}_{-0.0302}$ | 0.072'/8.00kpc |
| 2 180103A | $71.43^{+26.84}_{-26.84}$ | $191.99^{+190.94}_{-190.94}$ | $52.22^{+82.50}_{-82.50}$ | $84.25^{+50.42}_{-50.42}$ | $4.39^{+5.09}_{-5.09}$ | AstroSAT ^I | $0.037^{+0.0063^a}_{-0.0015}$ | 0.184'/8.75kpc |
| 3 180427A | $60.01^{+22.32}_{-22.32}$ | $7.03^{+6.61}_{-6.61}$ | $1.89^{+2.88}_{-2.88}$ | $2.87^{+1.74}_{-1.74}$ | $4.08^{+4.57}_{-4.57}$ | AstroSAT ^I | $0.0309^{+0.045^a}_{-0.0309}$ | 0.273'/10.81kpc |
| 4 200412A | < 53.84 | $1611.02^{+1649.92}_{-1649.92}$ | $532.48^{+734.13}_{-734.13}$ | $419.58^{+320.89}_{-320.89}$ | $2.61^{+3.33}_{-3.33}$ | AstroSAT ^I | $0.1055^{+0.0192^a}_{-0.0145}$ | 0.131'/18.74kpc |
| 5 061122A | 11^{+48}_{-11} | $96.39^{+65.43}_{-65.43}$ | $28.59^{+23.40}_{-23.40}$ | $11.80^{+12.22}_{-12.22}$ | $1.22^{+1.52}_{-1.52}$ | INTEGRAL ^{II} | $1.33^{+0.77^b}_{-0.76}$ | 0.435"/20.13kpc |
| 6 200806A | < 54.73 | $83.06^{+56.35}_{-56.35}$ | $32.10^{+26.47}_{-26.47}$ | $3.64^{+4.85}_{-4.85}$ | $0.44^{+0.65}_{-0.65}$ | AstroSAT ^I | $0.1148^{+0.1749^a}_{-0.1148}$ | 0.234'/36.58kpc |

TABLE II: The list of GRBs with candidate host galaxies and their associated properties. I, II, *, a, b is the same as in Table I.

photospheric models with dissipation [52]. However, the issues remain controversial. The observed spectra are frequently fitted using the Band function [53], which is described by three key parameters: the spectral peak energy E_p , the low-energy spectral index α_s , and the high-energy spectral index β_s . Ref. [51] have found a potential negative correlation between Π_L and E_p arising from synchrotron emission within a globally ordered magnetic field. Here, we also list Π_L and the corresponding band function parameters for our sample in Table I. A significant portion of the parameters is obtained from Ref. [42], followed by Ref. [54], Ref. [43], and Ref. [45]. Meanwhile, we add the fluence⁴ for each GRB to Table I. Furthermore, we analyze the potential correlation between Π_L and these parameters as shown in Fig. 3, where red dots represent sources with Π_L , and black dots represent sources with only the upper or lower limit of Π_L . Spearman correlation coefficients r_s are exclusively derived from the red dots. Fig. 3(a) illustrates the data points of Π_L vs. α_s . All α_s are distributed between -1.4 to -0.2 . About half of them are concentrated around -0.85 . The Spearman correlation coefficient is $r_s = -0.11 \pm 0.45$. In Fig. 3(b), the data points of Π_L vs. β_s are presented, with $r_s = 0.19 \pm 0.44$. The distribution of all β_s values falls within the range of -3.5 to -1.5 . Most of them are concentrated around -2.5 . Fig. 3(c) shows the data points of Π_L vs. E_p , with $r_s = 0.16 \pm 0.45$. These data points are scattered within the range of 50 keV to 1250 keV. Most of them are less than 500 keV. The Band function has a smoothly broken power law with spectral peak energy at $E_p \simeq 210$ keV in νF_ν space, featuring asymptotic power-law photon indices below ($\alpha_s \simeq -0.8$) and above ($\beta_s \simeq -2.5$) the break energy [51, 55]. Our α_s and β_s match the features, but E_p is not evident. In Fig. 3(d), the data points of Π_L vs. Fluence are shown, with $r_s = -0.03 \pm 0.48$. They all fall between 1×10^{-6} erg cm⁻² and 6.5×10^{-4} erg cm⁻². The data points are widely dispersed, with all correlation coefficient absolute values obtained being less than 0.3.

Meanwhile, the errors associated with these coefficients exceed the coefficients themselves. Consequently, it is not possible to determine whether there exists a correlation between Π_L and the spectral parameters, limiting our ability to confirm or rule out the correlation predicted by Ref. [51].

The inclusion of photon-ALP mixing further complicates this issue, particularly when considering mixing within the inner structure of GRBs. However, the precise location of photon-ALP mixing within the source remains elusive. Some studies suggest that mixing occurs in the external shock [4] with \mathbf{B}_{jet} around $\mathcal{O}(1)$ G, while others explore the possibility of mixing in the internal shock with \mathbf{B}_{jet} ranging from 10^6 G [36] to 10^9 G [37]. It is imperative to thoroughly investigate potential deviations in both the early-time evolution pattern of Π_L and the spectral shape from predictions made by traditional emission models. However, it is important to note that the detected Π_L values, as depicted in Fig. 1, are averaged over both energy and time. In the future, with the discovery of closer sources and the minimization of the influence of \mathbf{B}_{IGM} , coupled with time-resolved high-sensitivity observations, there exists the possibility of more accurately probing the impact of the magnetic field within the source. In the current paper, our focus will be on assessing the influence of \mathbf{B}_{IGM} on the initial Π_L .

C. Π_L vs. Host Galaxies' Properties

The intrinsic characteristics of a GRB itself may contribute to the variability of Π_L , while the properties of the GRB host galaxies could also influence Π_L . To explore this possibility, we analyzed the photometric data obtained from six candidate host galaxies of GRBs, as listed in Table II. Utilizing Spectral Energy Distribution (SED) fitting via the CIGALE code, we derived various galactic properties, including the stellar mass (M_\star), gas mass (M_{gas}), star formation rate (SFR), specific star formation rate (sSFR) for these candidate host galaxies. The results of this analysis are presented in Table II. We then investigated the potential correlation between

⁴ https://user-web.icecube.wisc.edu/~grbweb_public/Summary_table.html

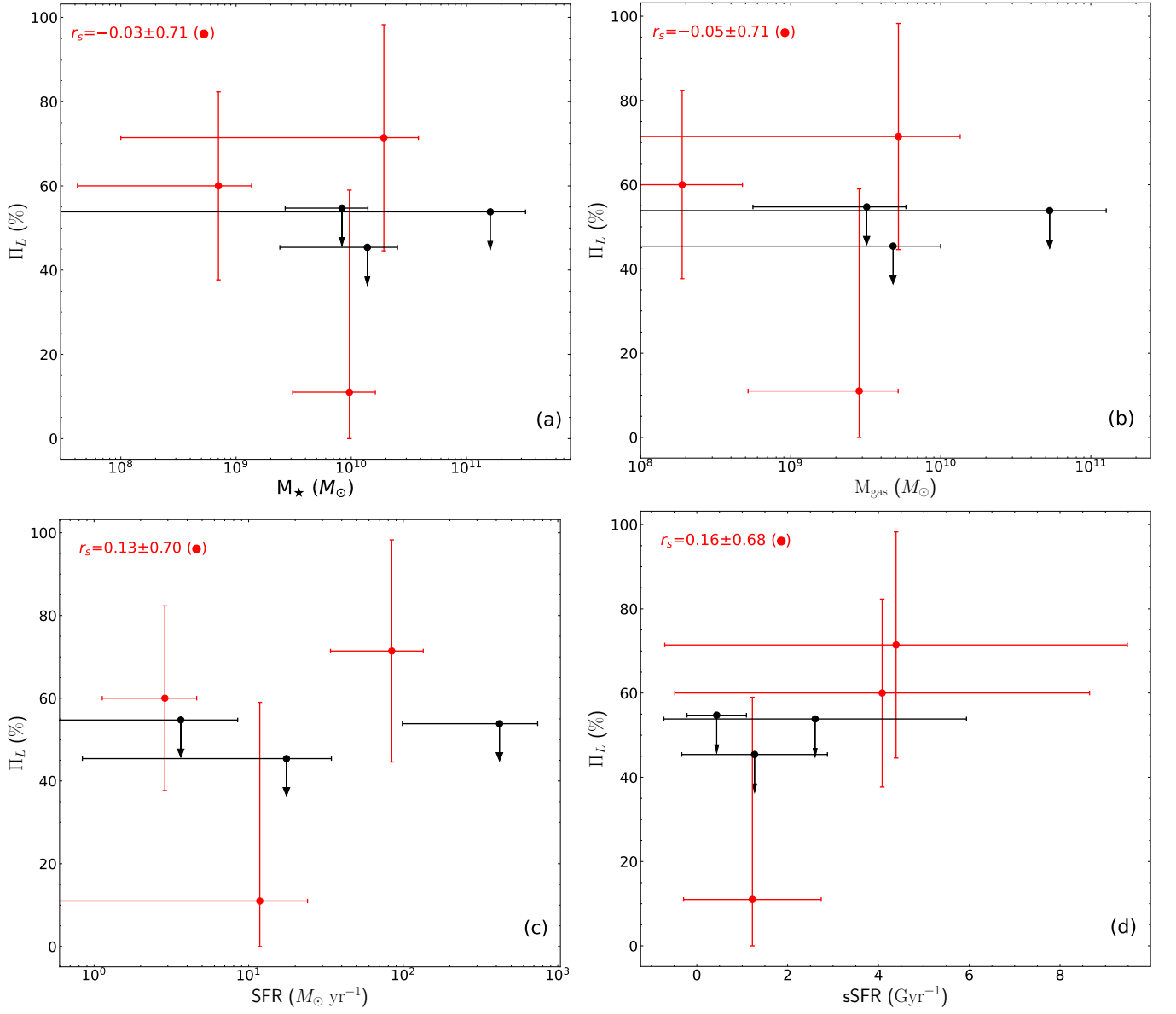


FIG. 4: Comparison between Π_L and the properties of the GRB candidate host galaxies. Red color denotes sources with measured Π_L , whereas black color represents sources with Π_L constrained as an upper limit. (a) Π_L vs. M_\star with $r_s = -0.03 \pm 0.71$. (b) Π_L vs. M_{gas} with $r_s = -0.05 \pm 0.71$. (c) Π_L vs. SFR with $r_s = 0.13 \pm 0.70$. (d) Π_L vs. sSFR with $r_s = 0.16 \pm 0.68$.

the measured Π_L and these galactic properties. The results are presented in Fig. 4. Red data points denote sources with Π_L , whereas black data points represent sources with an upper limit of Π_L . Correlation calculations exclusively utilized the red data points.

Fig. 4(a) displays comparison between the measured Π_L and M_\star . The latter of the candidate host galaxies for GRBs ranges between $6 \times 10^8 M_\odot$ and $2 \times 10^{11} M_\odot$, with approximately half centered around $10^{10} M_\odot$, smaller than that in the Milky Way. The Spearman correlation coefficient $r_s = -0.03 \pm 0.71$. Extinction (A_v) for candidate host galaxies was also calculated, with only one showing a small extinction close to 1, while the rest

exhibit zero extinction. This low or zero extinction suggests a limited amount of dust present in these galaxies. Fig. 4(b) displays comparison between the measured Π_L and M_{gas} . All M_{gas} of the candidate host galaxies for GRBs span from $10^8 M_\odot$ to $10^{11} M_\odot$, with a majority clustered around $4 \times 10^9 M_\odot$. Distribution of M_{gas} resembles that of M_\star and the Spearman correlation coefficient is $r_s = -0.05 \pm 0.71$. Fig. 4(c)/(d) demonstrates a comparison between the measured Π_L and SFR/sSFR in the candidate host galaxies. The Spearman correlation coefficient is $r_s = 0.13 \pm 0.70 / r_s = 0.16 \pm 0.68$. The majority of SFR values are less than tens of $M_\odot \text{ yr}^{-1}$ with a single exception displaying a value of several hun-

dred $M_\odot \text{ yr}^{-1}$, akin to starburst galaxies. All sSFRs are under 5 Gyr^{-1} . The absolute values of the above Spearman correlation coefficients are all less than 0.2 based on the limited sample and the significant uncertainties. We are unable to draw any conclusions about the correlation between the measured Π_L and these galactic properties. However, we can infer that with diversity in the properties of candidate host galaxies, the Π_L of emission from GRB's prompt phase could become more diverse, especially when considering the photon-ALP mixing in the host magnetic fields \mathbf{B}_{host} . Hence, we do not consider the influence of \mathbf{B}_{jet} or \mathbf{B}_{host} , our focus will be on assessing the influence of \mathbf{B}_{IGM} on the initial linear polarization degree (Π_{L0}), which refers to the polarization state of photons emitted by GRBs as they enter the intergalactic medium.

D. Π_L vs. GRBs' Redshifts

The correlation between spectral slope and redshift in the observed γ -ray spectra of blazars has been considered as an indication of photon-ALP mixing in \mathbf{B}_{IGM} [21–23]. It is worth exploring whether the same pattern may also exist among the data points of the measured Π_L and redshifts, which are shown in Fig. 5. The Spearman correlation coefficient obtained from sources with confirmed polarization values is $r_s = -0.18 \pm 0.45$, indicating a lack of statistical behavior in describing the evolution of measured Π_L over redshift. In the context of photon-ALP mixing in \mathbf{B}_{IGM} , we could still utilize the distribution of the measured Π_L with redshifts to impose constraints on the mixing, or to explore the allowing parameter space of ALPs and \mathbf{B}_{IGM} that could allow us to safely ignore the propagation effects on the Π_{L0} .

III. PHOTON-ALP MIXING

A. Basic model

This section will illustrate the basic framework related to photon-ALP mixing in external magnetic fields. The Lagrangian of photon-ALP coupling is generally described by the following equation:

$$\mathcal{L}_{a\gamma} = -\frac{1}{4} g_{a\gamma} F_{\mu\nu} \tilde{F}^{\mu\nu} a = g_{a\gamma} \mathbf{E} \cdot \mathbf{B} a, \quad (2)$$

where $F_{\mu\nu}$ and $\tilde{F}^{\mu\nu}$ are the electromagnetic field tensor and its dual, respectively. We initiate our analysis with a photon beam propagating along the x_3 -direction. The beam propagation equation can be written in the following Schrödinger-like one

$$\left(i \frac{d}{dx_3} + E + \mathcal{M} \right) \begin{pmatrix} A_{x_1}(x_3) \\ A_{x_2}(x_3) \\ a(x_3) \end{pmatrix} = 0, \quad (3)$$

where E is the energy of photon-ALP beam, \mathcal{M} is the photon-ALP mixing matrix, $A_{x_1}(x_3)$ and $A_{x_2}(x_3)$ are the photon linear polarization amplitudes along the x_1 and x_2 axis, respectively, and $a(x_3)$ is the ALP amplitude. ALPs and photon couple in the transverse magnetic field \mathbf{B}_T , namely magnetic field component in the x_1 - x_2 plane.

The angle formed by \mathbf{B}_T and x_2 -axis is ψ . When ψ is 0, the mixing matrix in the homogeneous magnetic field can be simplified to [37]

$$\mathcal{M}^{(0)} = \begin{pmatrix} \Delta_\perp & 0 & 0 \\ 0 & \Delta_\parallel & \Delta_{a\gamma} \\ 0 & \Delta_{a\gamma} & \Delta_a \end{pmatrix}, \quad (4)$$

where

$$\begin{aligned} \Delta_{a\gamma} &\equiv \frac{1}{2} g_{a\gamma} B_T \\ &\simeq 1.5 \times 10^{-2} \frac{g_{a\gamma}}{10^{-11} \text{ GeV}^{-1}} \frac{B_T}{\text{nG}} \text{ Mpc}^{-1}, \\ \Delta_a &\equiv -\frac{m_a^2}{2E} \\ &\simeq -7.8 \times 10^{-3} \left(\frac{m_a}{10^{-13} \text{ eV}} \right)^2 \left(\frac{E}{10^2 \text{ keV}} \right)^{-1} \text{ Mpc}^{-1}, \\ \Delta_{\text{pl}} &\equiv -\frac{\omega_{\text{pl}}^2}{2E} \\ &\simeq -1.1 \times 10^{-4} \left(\frac{E}{10^2 \text{ keV}} \right)^{-1} \frac{n_e}{10^{-7} \text{ cm}^{-3}} \text{ Mpc}^{-1}, \\ \Delta_{\text{QED}} &\equiv \frac{\alpha E}{45\pi} \left(\frac{B_T}{B_{\text{cr}}} \right)^2 \\ &\simeq 4.1 \times 10^{-16} \frac{E}{10^2 \text{ keV}} \left(\frac{B_T}{10^{-9} \text{ G}} \right)^2 \text{ Mpc}^{-1}, \\ \Delta_\parallel &\equiv \Delta_{\text{pl}} + 3.5 \Delta_{\text{QED}}, \quad \Delta_\perp \equiv \Delta_{\text{pl}} + 2 \Delta_{\text{QED}}. \end{aligned} \quad (5)$$

After traveling a distance of d , the probability of the photon's initial linear polarization along the x_2 -axis transforming into ALPs is

$$P_{\gamma \rightarrow a}^{(0)} = \sin^2 2\theta \sin^2 \left(\frac{\Delta_{\text{osc}} d}{2} \right), \quad (6)$$

where the oscillation wave number is

$$\Delta_{\text{osc}} = \left[(\Delta_a - \Delta_\parallel)^2 + 4\Delta_{a\gamma}^2 \right]^{1/2} \quad (7)$$

and the mixing angle is

$$\theta = \frac{1}{2} \arctan \left(\frac{2\Delta_{a\gamma}}{\Delta_\parallel - \Delta_a} \right). \quad (8)$$

When $\sin^2 2\theta \simeq 1$, that is $\theta \simeq \pi/4$, photon-ALP oscillations reach their maximum. This condition is then determined by

$$|\Delta_\parallel - \Delta_a| \ll 2\Delta_{a\gamma}. \quad (9)$$

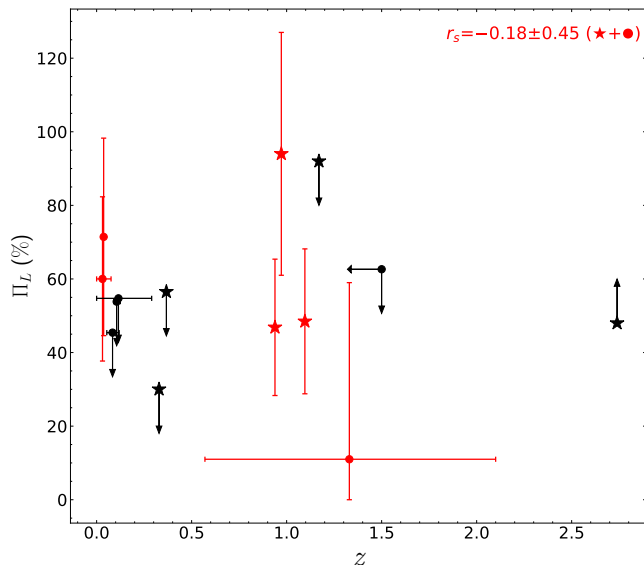


FIG. 5: Comparison between Π_L and redshifts of the GRBs. The pentagon denotes sources with spectroscopic redshift, while the dot represents sources without spectroscopic redshift, as well as sources with only upper limits on their redshift. The correlation coefficients are $r_s = -0.18 \pm 0.45$ for the red ones.

If the Δ_{QED} term could be ignored where $\mathbf{B}_T \ll \mathbf{B}_{cr} \simeq 4.41 \times 10^{13}$ G, $\Delta_{\parallel} \simeq \Delta_{\perp} \simeq \Delta_{\text{pl}}$. We then can define a low energy limit as

$$E_L \equiv \frac{E |\Delta_a - \Delta_{\text{pl}}|}{2 \Delta_{a\gamma}} \simeq \frac{25 |m_a^2 - \omega_{\text{pl}}^2|}{(10^{-13} \text{eV})^2} \left(\frac{\text{nG}}{B_T} \right) \left(\frac{10^{-11} \text{GeV}^{-1}}{g_{a\gamma}} \right) \text{keV}. \quad (10)$$

If \mathbf{B}_T approaches \mathbf{B}_{cr} , a high energy limit defined as

$$E_H \equiv \frac{90\pi g_{a\gamma} B_{cr}^2}{7\alpha B_T} \simeq 2.1 \times 10^{15} \left(\frac{\text{nG}}{B_T} \right) \left(\frac{g_{a\gamma}}{10^{-11} \text{GeV}^{-1}} \right) \text{keV}. \quad (11)$$

When $E_L \ll E \ll E_H$, photon-ALP oscillations reach their maximum (generally called strong mixing), and the conversion probability becomes energy-independent. The above-associated plasma frequency

$$\omega_{\text{pl}} = \sqrt{4\pi\alpha n_e/m_e} = 3.71 \times 10^{-14} \sqrt{\frac{n_e}{\text{cm}^3}} \text{keV}, \quad (12)$$

where n_e is the electron density in the medium.

Moreover, the initial polarization state of the photon is expected to change as a result of its interaction with spin-zero ALPs. Typically, we employ the Stokes parameters

to characterize the polarization state, defined as follows:

$$\begin{aligned} I &= \langle A_{x_2}^*(x_3) A_{x_2}(x_3) \rangle + \langle A_{x_1}^*(x_3) A_{x_1}(x_3) \rangle, \\ Q &= \langle A_{x_2}^*(x_3) A_{x_2}(x_3) \rangle - \langle A_{x_1}^*(x_3) A_{x_1}(x_3) \rangle, \\ U &= 2\text{Re} \langle A_{x_2}^*(x_3) A_{x_1}(x_3) \rangle, \\ V &= 2\text{Im} \langle A_{x_2}^*(x_3) A_{x_1}(x_3) \rangle, \end{aligned} \quad (13)$$

where $A_{x_1}^*(x_3)$ ($A_{x_2}^*(x_3)$) is the conjugation of $A_{x_1}(x_3)$ ($A_{x_2}(x_3)$). The linear polarization degree Π_L can be expressed by stokes parameters as

$$\Pi_L = \frac{\sqrt{Q^2 + U^2}}{I}. \quad (14)$$

In the literature, it is more convenient to use the polarization density matrix and its transfer matrix for numerical calculation. The polarization density matrix is defined as [37]

$$\rho(x_3) = \begin{pmatrix} A_{x_1}(x_3) \\ A_{x_2}(x_3) \\ a(x_3) \end{pmatrix} \otimes \left(A_{x_1}(x_3) \ A_{x_2}(x_3) \ a(x_3) \right)^*, \quad (15)$$

which obeys the Liouville-Von Neumann equation

$$i \frac{d\rho}{dx_3} = [\rho, \mathcal{M}]. \quad (16)$$

We use $T(x_3, x_3^0)$ to represent the transfer matrix. Then $T(x_3^0, x_3^0) = 1$ is the initial condition for solution of Eq. (3). The solution of Eq. (16) can be expressed by the transfer equation as follows [37]

$$\rho(x_3) = T(x_3, x_3^0) \rho(x_3^0) T^\dagger(x_3, x_3^0). \quad (17)$$

The comprehensive procedure for solving $\rho(x_3)$ is not outlined here. For a detailed derivation of $\rho(x_3)$, refer to Section 3 of Ref. [37], specifically equations (9) to (42). The detailed derivation of the expressions of stokes parameters in terms of the polarization density matrix is also presented in Ref. [56]. We give the final expression of the 2×2 photon polarization density matrix (i.e. the 1-2 block of the density matrix for the photon-ALP system) here:

$$\rho_\gamma = \frac{1}{2} \begin{pmatrix} I + Q & U - iV \\ U + iV & I - Q \end{pmatrix}, \quad (18)$$

and the linear polarization degree is then expressed as follows:

$$\Pi_L \equiv \frac{\sqrt{Q^2 + U^2}}{I} = \frac{\sqrt{(\rho_{11} - \rho_{22})^2 + (\rho_{12} + \rho_{21})^2}}{\rho_{11} + \rho_{22}}. \quad (19)$$

Through this paper, we utilize the gammaALPs tool, publicly accessible at <https://gammaalps.readthedocs.io/en/latest/>, to numerically solve the transfer equation for photon-ALP

mixing. This code is specifically designed to handle complex scenarios involving diverse initial states and arbitrary orientations of \mathbf{B}_T with an angle ψ relative to the x_2 -axis within different magnetic configurations. The photon-ALP beam, during its propagation from the source to Earth, can traverse various magnetic fields including those associated with the source (eg \mathbf{B}_{jet}), the host galaxy (\mathbf{B}_{host}), the intergalactic medium (\mathbf{B}_{IGM}), and the Milky Way (\mathbf{B}_{MW}). If located within a galaxy cluster, the photon-ALP beam would also traverse the magnetic field of the intra-cluster medium (\mathbf{B}_{ICM}).

B. Basic parameters

In Sec. II, we have explored the statistical characteristics of Π_L . Predictions for Π_L from numerical simulations of popular emission mechanisms during the prompt phase of GRBs range from as low as 4% to values exceeding 80%. Uncertainties regarding the jet structure and the diverse properties of host galaxies further complicate this issue, particularly in the context of photon-ALP mixing within \mathbf{B}_{jet} and/or \mathbf{B}_{host} . Therefore, we consider the polarization state of photons emitted by GRBs as they enter the intergalactic medium as our initial Π_{L_0} , which ranges from unpolarized case ($\Pi_{L_0} = 0$) to fully linearly polarized case ($\Pi_{L_0} = 100\% = 1$), focusing our analysis on the influence of \mathbf{B}_{IGM} and \mathbf{B}_{MW} on the Π_{L_0} for GRBs across varied redshifts.

For \mathbf{B}_{IGM} , our current understanding is very limited. Observations of Faraday rotation in both radio and optical wavelengths from distant astronomical sources have revealed the presence of weak yet coherent magnetic fields in extragalactic space. However, the origin, intensity, and configuration of these magnetic fields remain subjects of ongoing research and debate [57]. The dynamical amplification of primordial seed fields, whether generated from the early universe or by motions of the plasma in (proto) galaxies, could, in principle, lead to the establishment of such a large-scale magnetic field. However, there is considerable uncertainty and complexity in the physical processes involved, making theoretical predictions highly uncertain. Meanwhile, a large region of the strength of \mathbf{B}_{IGM} has been obtained in observations. The lower limits for \mathbf{B}_{IGM} can be obtained based on the electromagnetic cascade generated by the deflection of electron-positron pairs by the \mathbf{B}_{IGM} with the value around the order of 10^{-14} G [58–61]. Faraday rotation measurements have imposed upper limits on \mathbf{B}_{IGM} around $\mathcal{O}(1)$ nG for coherence lengths of about $\mathcal{O}(1)$ Mpc, while the bound decreases with the increasing correlation length [62]. The above limits on the strength of \mathbf{B}_{IGM} are deduced from limited observational data. Precise measurements remain challenging due to the diffuse and low-density nature of the intergalactic medium. In the scenario of photon-ALP mixing, the \mathbf{B}_{IGM} approaching the current upper limit are typically assumed to investigate the maximum potential effects. In Ref. [63], numerical

calculations showed that the impact of photon-ALP mixing increases with the intensity of \mathbf{B}_{IGM} among the strong mixing energy region. As indicated by Eq. (7), when $E_L \ll E \ll E_H$, photon-ALP mixing becomes energy-independent, with the mixing term $\Delta_{a\gamma} \equiv \frac{1}{2}g_{a\gamma}\mathbf{B}_{\text{IGM}}$ serving as the key factor reflecting the strength of the induced effects. Any constraints on the mixing effect can, in turn, be regarded as constraints on $g_{a\gamma}\mathbf{B}_{\text{IGM}}$. Here, we adopt that $\mathbf{B}_{\text{IGM}} = 1$ nG and coherence length $L_{\text{coh}} = 1$ Mpc at $z = 0$. For n_e in the intergalactic medium, we use the typical values 10^{-7}cm^{-3} derived from the baryon density [64] and the corresponding plasma frequency is 1.17×10^{-14} eV as calculated with Eq. (12). Regarding the configuration of \mathbf{B}_{IGM} , a conventional domain-like model is commonly utilized. In this model, the magnetic field strength remains constant within each domain, while the direction changes randomly from one domain to another. Ref. [38] compare this traditional domain-like model with another domain-like model, wherein the magnetic field is helical within each domain. They argue that these two models show a similar asymptotic behavior. Here, we follow the steps in Ref. [65] and adopt the conventional domain-like model. To achieve this, we treat ψ as a random variable in the range of 0 to 2π for each domain with size L_{coh} and constant \mathbf{B}_{IGM} . As the photon beam travels along the x_3 -axis from the source to the observer, it will experience a series of random magnetic field domains. One set of ψ values means one realization of the random magnetic field configurations.

For \mathbf{B}_{WM} , we have a more comprehensive understanding of its morphology. We consider the model developed by Jansson and Farrar to be a well-established one [4, 66–68]. The photons of GRBs from different lines of sight undergo different parts of the magnetic fields during their propagation within the Milky Way. If the mixing in the Galactic magnetic field is significant, it is anticipated that the effects of mixing would vary depending on Galactic positions of the GRBs. However, as we examine later, mixing in \mathbf{B}_{WM} is negligible within the parameter space of ALP and the energy band we are exploring.

Another crucial set of parameter is m_a and $g_{a\gamma}$. The most reliable constraints on ALPs come from the none detection of ALPs from the Sun derived by the CERN Axion Solar Telescope (CAST), yielding an upper limit for $g_{a\gamma}$ as 6.6×10^{-11} GeV $^{-1}$ for $m_a \lesssim 0.02$ eV [69]. For m_a values considerably exceeding the plasma frequency ω_{pl} , the mass term will predominate over the mixing term. Conversely, for m_a values much less than ω_{pl} , they could then be safely ignored, and the mixing effects would be independent of the value of m_a as indicated in Eq. (6–10). Considering that the measured value of the time-integrated linear polarization (Π_L) we are focusing on is in the sub-MeV energy range and the plasma frequency of the intergalactic medium under our consideration is $\omega_{\text{pl}} \simeq 1.17 \times 10^{-14}$ eV, as indicated by E_L , to ensure that photon-ALP mixing occurs within the strong mixing regime, we will use $g_{a\gamma} = 0.5 \times 10^{-11}$ GeV $^{-1}$ for $m_a \leq 10^{-14}$ eV as our benchmark model parameters.

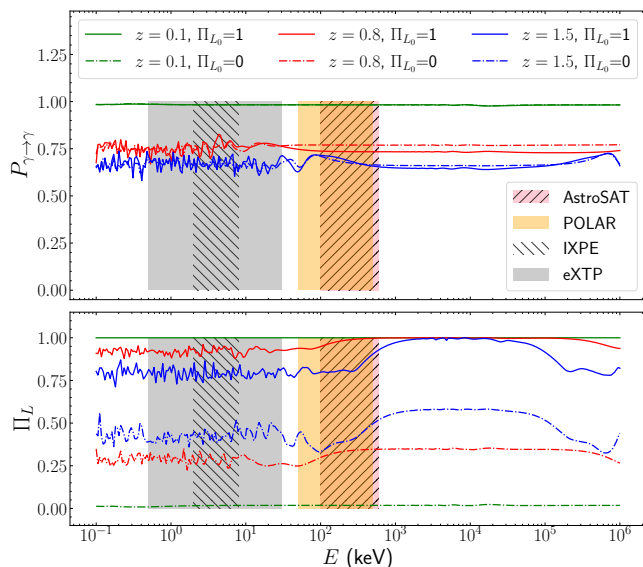


FIG. 6: Average final photon survival probability $P_{\gamma \rightarrow \gamma}$ (upper panel) and average final linear polarization degree Π_L (lower panel) as a function of photon energy E for ALP with $m_a = 10^{-14}$ eV and $g_{a\gamma} = 0.5 \times 10^{-11}$ GeV $^{-1}$. Green, red, and blue lines denote source redshifts of 0.1, 0.8, and 1.5, respectively. Solid and dash-dotted lines represent $\Pi_{L_0}=1$ and $\Pi_{L_0}=0$, respectively. Shadow zones denote energy bands for various polarimeters: AstroSAT (shaded pink), POLAR (orange), IXPE (shaded black), and eXTP (grey).

IV. RESULTS

This section presents our results using the elaborated parameters set above. Firstly, we consider ALPs with $m_a = 10^{-14}$ eV and $g_{a\gamma} = 0.5 \times 10^{-11}$ GeV $^{-1}$ to explore the primary features of the potential effects induced by photon-ALP mixing in the extragalactic medium. All calculations presented here have been conducted with mixing in \mathbf{B}_{IGM} and \mathbf{B}_{MW} . However, we have examined sources from different lines of sight, e.g., Galactic latitudes b ranging from 10° , 40° , to 60° , and found no significant differences in the results. Therefore, in the sub-MeV energy band with the benchmark model we consider, variations induced by \mathbf{B}_{MW} can be disregarded.

In Fig. 6, we display the photon survival probability $P_{\gamma \rightarrow \gamma}(E)$ (upper panel) and the linear polarization degree $\Pi_L(E)$ (lower panel) for initially unpolarized photons ($\Pi_{L_0} = 0$, dash-dotted lines) and fully linearly polarized photons ($\Pi_{L_0} = 1$, solid lines) emitted at three typical redshifts, each indicated by a different color. $P_{\gamma \rightarrow \gamma}$ maintains its independence of photon energy E , as anticipated in cases of strong mixing. The photon flux remains unchanged for low redshift ($z=0.1$) while decreasing 20% for medium redshift ($z=0.8$) and 40% for high redshift ($z=1.5$) irrespective of their initial polarization states. The asymptotic trend of $P_{\gamma \rightarrow \gamma}$ approaching $2/3$ for high-redshift sources is foreseeable when photon-ALP beams traverse a sufficient number of domains [37, 38].

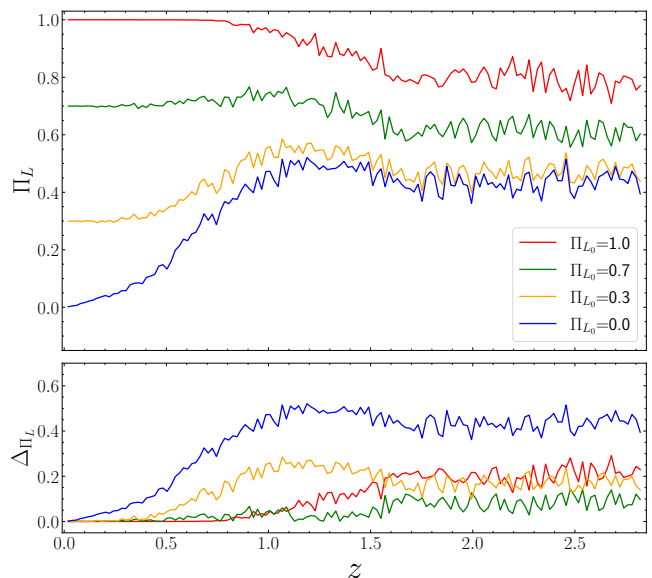


FIG. 7: Average final Π_L (upper panel) and Δ_{Π_L} (lower panel) as a function of the source redshift z for ALP with $m_a = 10^{-14}$ eV and $g_{a\gamma} = 0.5 \times 10^{-11}$ GeV $^{-1}$ and photon energy $E = 350$ keV. Colors indicate different Π_{L_0} : 1.0 (red), 0.7 (green), 0.3 (orange), 0.0 (blue).

$\Pi_L(E)$ exhibits similarities with the observed features in $P_{\gamma \rightarrow \gamma}(E)$ regarding energy. The modifications as defined by $\Delta_{\Pi_L} \equiv |\Pi_L - \Pi_{L_0}|$ are different for different initial polarization states assumed. For the low-redshift source ($z=0.1$), the modifications induced by the photon-ALP mixing are negligible as shown by the green lines in the bottom panel; the source maintains its initial polarization state. For sources at higher redshifts, photon-ALP mixing leads to a decrease in the polarization degree of initially fully linearly polarized photons, while it induces a certain degree of polarization to initially unpolarized photons. The magnitude of this alteration increases with higher redshift. In the keV to MeV energy range, at $z=0.8$, Δ_{Π_L} for $\Pi_{L_0} = 1.0$ is about 0.1, while at $z=1.5$, it is approximately 0.2. At $z=0.8$, the polarization degree of unpolarized photons increases to 0.3, whereas at $z=1.5$, it increases to around 0.4. While these specific values correspond to the averaged values over 50 realizations of the orientations of the series domains of \mathbf{B}_{IGM} , these case studies have revealed the trend that alterations to Π_{L_0} could be significant for our benchmark model. We also note that for photons with energies greater than MeV, these changes in the unpolarized case become more pronounced. As our study focuses on the sub-MeV energy range, we do not delve further into this aspect.

In Fig. 6, we have also marked the relevant energy bands of the high-energy polarimeters as shadowed areas. The shaded pink, orange, shaded black, and grey shadow zone represent AstroSAT, POLAR, IXPE, and eXTP, respectively. As illustrated in Table. I, most of the mea-

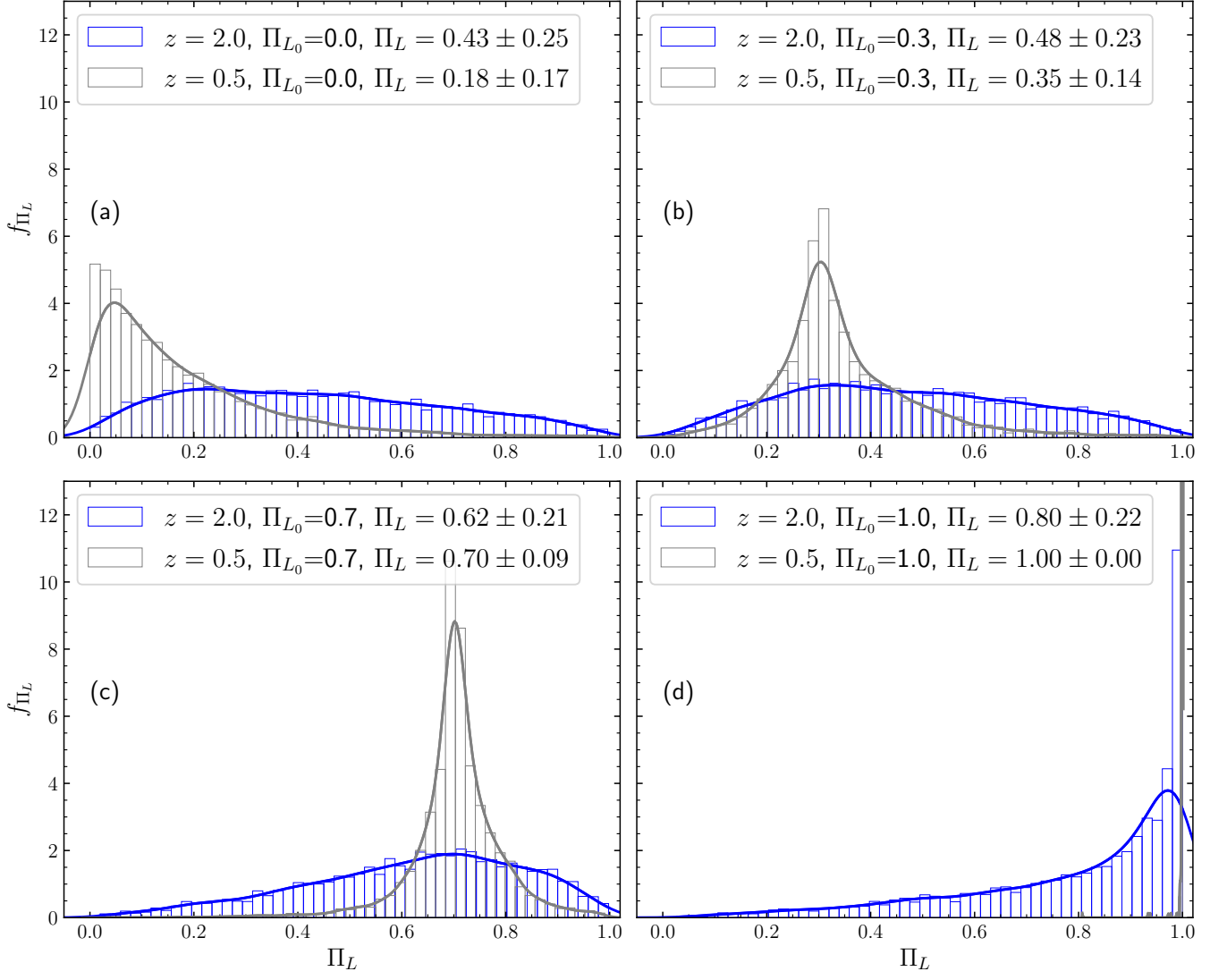


FIG. 8: Probability density function f_{Π_L} of Π_L for ALP with $m_a=10^{-14}$ eV and $g_{a\gamma}=0.5 \times 10^{-11}$ GeV $^{-1}$ and photon energy $E = 350$ keV. Blue and grey represent sources at redshift $z = 2.0$ and 0.5 , respectively. In (a), (b), (c), and (d), for $z = 2.0$, the mean final $\Pi_L=0.43 \pm 0.25$ ($\Pi_{L_0} = 0.0$), $\Pi_L=0.48 \pm 0.23$ ($\Pi_{L_0} = 0.3$), $\Pi_L=0.62 \pm 0.21$ ($\Pi_{L_0} = 0.7$), $\Pi_L=0.80 \pm 0.22$ ($\Pi_{L_0} = 1.0$); for $z = 0.5$, $\Pi_L=0.18 \pm 0.17$ ($\Pi_{L_0} = 0.0$), $\Pi_L=0.35 \pm 0.14$ ($\Pi_{L_0} = 0.3$), $\Pi_L=0.70 \pm 0.09$ ($\Pi_{L_0} = 0.7$), $\Pi_L=1.00 \pm 0.00$ ($\Pi_{L_0} = 1.0$).

sured Π_L with possible redshift identified are obtained by AstroSAT, which covers the 100-600 keV energy band. Hence, we will choose the middle-energy $E = 350$ keV to account for the measured photon energy and we further explore the alternations to Π_{L_0} induced by photon-ALP mixing for this specific energy.

As analytically deduced in Ref. [38], there is an asymptotic behavior for Π_L when photons emitted from high-redshift GRBs are initially fully linearly polarized. Here, we present our numerical results of $\Pi_L(z)$ and $\Delta_{\Pi_L}(z)$ for a range of Π_{L_0} values as indicated by different colors in Fig. 7. In our results, this asymptotic behavior occurs across all the assumed Π_{L_0} values. For $\Pi_{L_0} = 0.0$ and $\Pi_{L_0} = 0.3$, representing low initial polarization degrees, Δ_{Π_L} exhibits a significant increase starting at a

redshift of approximately 0.5, reaching a maximum deviation close to 0.5, and stabilizing after redshift 1.7. For $\Pi_{L_0} = 0.7$ and $\Pi_{L_0} = 1.0$, representing high initial polarization degrees, visible increments begin around a redshift of approximately 1.0, with a maximum deviation close to 0.2, also stabilizing after redshift 1.7. From the upper panel, we can see that for sources at redshifts greater than 0.5, nearly all the photons exhibit Π_L above 0.2, regardless of their initial polarization state. However, as indicated in Fig. 1, 12 out of 50 observed GRBs have a measured Π_L less than 0.2, with none having a confirmed redshift yet. Further confirmation of the distances of these sources could potentially impose strong constraints on the photon-ALP mixing.

The averaged values of Π_L presented above are cal-

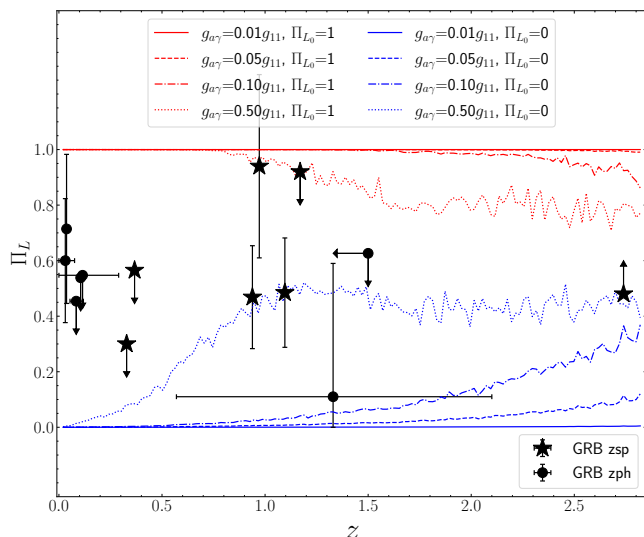


FIG. 9: Average final Π_L as a function of the source redshift z for ALP with $m_a = 10^{-14}$ eV and photon energy $E = 350$ keV. Red/blue line represents $\Pi_{L_0} = 1.0/0.0$. The different line styles represent different $g_{a\gamma}$, i.e., 0.01×10^{-11} GeV $^{-1}$ (solid line), 0.05×10^{-11} GeV $^{-1}$ (dashed line), 0.1×10^{-11} GeV $^{-1}$ (dash-dotted line), 0.5×10^{-11} GeV $^{-1}$ (dotted line), and $g_{11} = 10^{-11}$ GeV $^{-1}$. The data points are the sources listed in Table I. The pentagon/dot denotes sources with/without spectroscopic redshift.

culated across 50 realizations of the random magnetic field configurations of \mathbf{B}_{IGM} . It is important to note that each photon-ALP beam can only encounter one configuration at a time, and individual realizations do not hold representative significance. However, through computing numerous realizations, we can derive its statistical characteristics. Therefore, we analyze the probability density function f_{Π} associated with Π_L based on 5000 realizations of random magnetic field configurations. The resulting f_{Π} and the corresponding mean value and standard deviation of Π_L are presented in Fig. 8, where (a), (b), (c), and (d) represent $\Pi_{L_0} = 0.0, 0.3, 0.7,$ and 1.0 , respectively. For redshift $z = 0.5$ (grey color), all f_{Π} presents a peak approaching its initial polarization state. For low initial polarization degrees, the mean values of Π_L show deviations as labeled in the figure, $\Pi_L = 0.18 \pm 0.17$ for $\Pi_{L_0} = 0.0$ and $\Pi_L = 0.35 \pm 0.14$ for $\Pi_{L_0} = 0.3$. For redshift $z = 2.0$ (blue color), all f_{Π} distributions appear rather flat, showing no clustering with the initial polarization state. The mean and 1σ values of Π_L are as follows: 0.43 ± 0.25 for $\Pi_{L_0} = 0.0$, 0.48 ± 0.23 for $\Pi_{L_0} = 0.3$, 0.62 ± 0.21 for $\Pi_{L_0} = 0.7$, and 0.80 ± 0.22 for $\Pi_{L_0} = 1.0$. Thus, the photon-ALP mixing in our benchmark model may smear out the initial polarization state of photons emitted from high-redshift sources. These results are consistent with the asymptotic behavior discussed in Fig. 7, indicating that averaging over 50 realizations is sufficient to capture the asymptotic behavior.

Our above calculations used a benchmark model of ALPs with $m_a = 10^{-14}$ eV and $g_{a\gamma} = 0.5 \times 10^{-11}$ GeV $^{-1}$. Since $m_a = 10^{-14}$ eV is smaller than $\omega_{\text{pl}} \simeq 1.17 \times 10^{-14}$ eV, the ALP mass term could be safely dropped from the mixing term. The photon-ALP mixing effect would be independent of the value of ALP mass for $m_a \lesssim 10^{-14}$ eV. For such kind of low-mass ALPs, we further explore to what extent, the alternations to Π_{L_0} are small enough to be negligible given different $g_{a\gamma}$ values. Fig. 9 shows the average final linear polarization degree Π_L as a function of source redshift for two scenarios: initially unpolarized photons ($\Pi_{L_0} = 0$, blue lines) and fully polarized photons ($\Pi_{L_0} = 1$, red lines). Different line styles represent different values of $g_{a\gamma}$. As the value of $g_{a\gamma}$ goes from 0.5×10^{-11} GeV $^{-1}$ (dotted lines), 0.1×10^{-11} GeV $^{-1}$ (dash-dotted lines), 0.05×10^{-11} GeV $^{-1}$ (dashed lines) down to 0.01×10^{-11} GeV $^{-1}$ (solid lines), the modifications induced by mixing tend to decrease as expected. For the smallest value of $g_{a\gamma}$ considered in this study, sources at any redshift may retain their initial linear polarization state, irrespective of the assumed values of Π_{L_0} . This feature can be further confirmed in Fig. 10, where we present f_{Π} (based on 5000 realizations of random magnetic field configurations) along with the corresponding mean value and standard deviation of Π_L . In comparison to our benchmark model, f_{Π} for $g_{a\gamma} = 0.01 \times 10^{-11}$ GeV $^{-1}$ peaks at the exact value of the initial polarization state, regardless of Π_{L_0} , even when the redshift is as high as 2.0. The effect induced by photon-ALP mixing could be safely ignored. This result, in turn, leads us to conclusion that the strongest constraints on the upper limit of $g_{a\gamma}$ reach the order of 10^{-13} GeV $^{-1}$.

The sources listed in Table I are marked as the data points in Fig. 9, where the pentagon (dot) denotes sources with spectroscopic redshift (possible photometric redshifts or upper limits). We have examined the correlation between the measured Π_L and the redshifts of GRBs as shown in Fig. 5, indicating the lack of statistical behavior probably due to the limited number of the data points and the larger uncertainties either in measured Π_L or in the redshift determination. Constraints may be set from individual cases. A plausibly extremely useful one could be the lowest Π_L (GRB061122A) in Fig. 9, but unfortunately, the redshift is a photometric one resembling its possible host candidate galaxy, which severely suffers from larger uncertainties that require further confirmation. A more precise measurement of the redshift with a low value of Π_L could impose strong constraints on the photon-ALP mixing term $\Delta_{a\gamma} \equiv \frac{1}{2} g_{a\gamma} B_{\text{IGM}}$. For a fixed value of $\mathbf{B}_{\text{IGM}} = 1$ nG, GRB061122A-like polarization measurements at least lead to the exclusion of our benchmark model $g_{a\gamma} = 0.5 \times 10^{-11}$ GeV $^{-1}$ for $m_a \lesssim 10^{-14}$ eV.

To ensure that the photon maintains its initial polarization state after propagation in the extragalactic space, the strongest constraints on the upper limit of $g_{a\gamma}$ possibly reach the order of 10^{-13} GeV $^{-1}$ for $\mathbf{B}_{\text{IGM}} = 1$ nG,

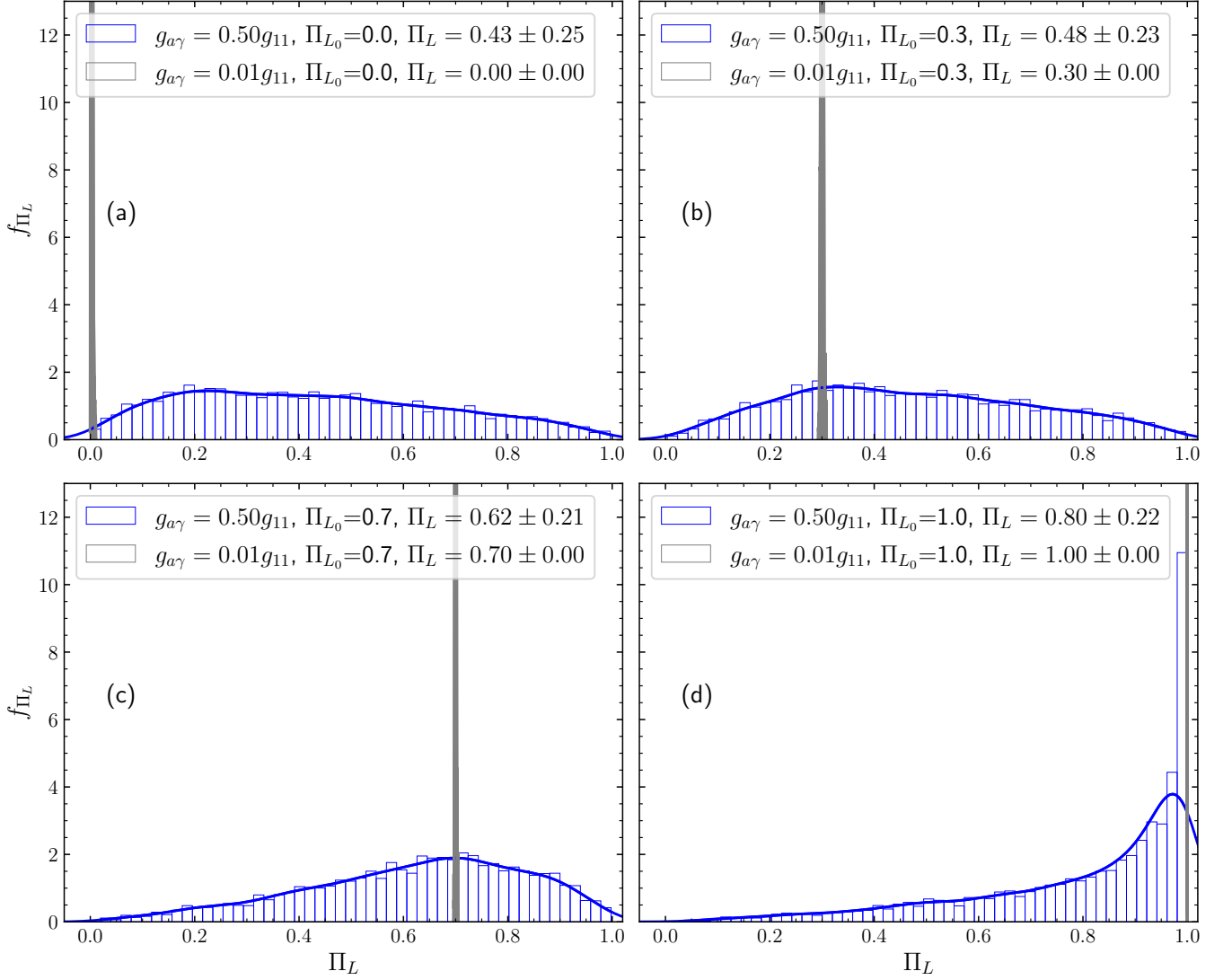


FIG. 10: Probability density function f_{Π_L} of Π_L for ALPs with $m_a=10^{-14}$ eV and photon energy $E = 350$ keV assuming a source at $z = 2$. $g_{11} = 10^{-11}$ GeV $^{-1}$. Blue and grey color represent $g_{a\gamma}=0.5 \times 10^{-11}$ GeV $^{-1}$ and 0.01×10^{-11} GeV $^{-1}$, respectively.

which means a requirement of the mixing term $\Delta_{a\gamma} = 1.5 \times 10^{-2} (g_{a\gamma}/10^{-11} \text{ GeV}^{-1}) (\mathbf{B}_{\text{IGM}}/\text{nG}) \text{ Mpc}^{-1} \leq 1.5 \times 10^{-4} \text{ Mpc}^{-1}$. Fig. 11 illustrates how the constraint on $g_{a\gamma}$ changes when \mathbf{B}_{IGM} is varied to different values. The solid/dashed/dotted line corresponds to $\mathbf{B}_{\text{IGM}} = 0.1/1.0/10.0$ nG. The colored regions represent several important constraints [69–72]. In the future, accurate measurements of \mathbf{B}_{IGM} could more precisely limit $g_{a\gamma}$, or conversely, measurements of $g_{a\gamma}$ could in turn provide independent checks on \mathbf{B}_{IGM} .

V. CONCLUSION AND DISCUSSION

In this work, we first examine the statistical characteristics of the measured time-integrated Π_L from differ-

ent polarimetric missions focusing on sub-MeV emissions. Our analysis reveals a diverse distribution of Π_L , which currently shows no correlation with spectral parameters or properties of candidate host galaxies. A thorough investigation of the redshift recognition has also been conducted to achieve a sample of 14 GRBs with both measured Π_L and redshift. The corresponding Spearman correlation coefficient is $r_s = -0.18 \pm 0.45$, indicating a lack of statistical behavior within the current sample due to large uncertainties in measured Π_L and redshift recognitions. Then we delve into the possible alternations $\Delta_{\Pi_L} \equiv |\Pi_L - \Pi_{L_0}|$ and present the primary features of the potential effects induced by photon-ALP mixing based on our fiducial model which satisfy current constraints on the ALP parameter space and \mathbf{B}_{IGM} . Photon-ALP mixing in the extragalactic space would further exaggerate

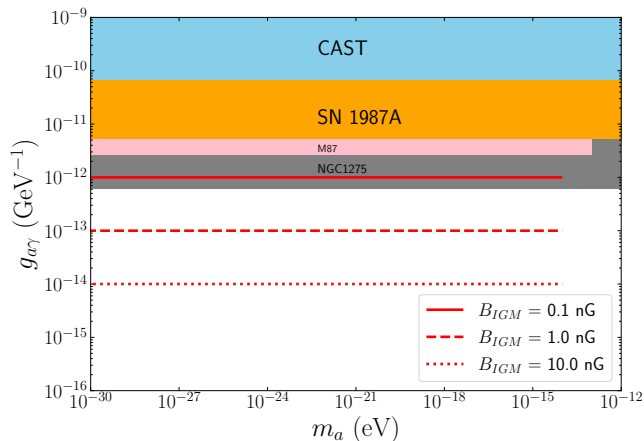


FIG. 11: Bounds on $g_{a\gamma}$ as $\Delta\Pi_L$ approaches to zero. The solid/dashed/dotted line corresponds to $\mathbf{B}_{IGM} = 0.1/1.0/10.0$ nG. The colored regions represent previously obtained bounds.

the diversity of Π_L and smear out the initial polarization state of the photons emitted by GRBs at high redshifts. To maintain the initial polarization state of a photon after traversing extragalactic space, the most stringent constraints on the upper limit of $g_{a\gamma}$ are on the order of 10^{-13} GeV^{-1} for $\mathbf{B}_{IGM} = 1$ nG, corresponding to a requirement that the mixing term $\Delta a\gamma$ be no greater than 1.5×10^{-4} Mpc^{-1} . In the future, better measurements of \mathbf{B}_{IGM} will impose secure limits on $g_{a\gamma}$, and conversely, good determination of $g_{a\gamma}$ will provide independent constraints on \mathbf{B}_{IGM} .

The lowest measured value ($\sim 11\%$) of Π_L with redshift recognition is GRB061122A but its photometric redshift ($z \sim 1.3$) suffers larger uncertainties that require further confirmation. Meanwhile, it is notable that 12 out of 50 observed GRBs have a measured Π_L less than 0.2, with none of them having a confirmed redshift yet. Further confirmation of the distances of these low- Π_L sources could potentially impose strong constraints on the photon-ALP mixing in extragalactic space. The ongoing polarimeter (CZTI) on-board AstroSAT is expected to increase the number of GRBs with measured Π_L and improve localization accuracy [42]. The forthcoming POLAR-2 [73] and the Large Area Burst Polarimeter (LEAP; [74]), operating in the energy range of 10 – 1000

keV, will significantly increase the number of GRBs observed across various redshifts. The statistical enhancement in the detection of high-energy polarization from GRBs, along with more accurate redshift verifications, is anticipated and thus better constraints on the mixing term will be achieved in the near future.

The most precise measurement of Π_L of GRBs is derived from observations of GRB221009A by IXPE. The small value of $\Pi_L = 0.06 \pm 0.03$ at 2–8 keV is attributed to dust-induced polarization within the Milky Way (indicated by days time-lag compared to its prompt phase), rendering it unsuitable for constraining mixing in IGM [50]. Persistent observations conducted by IXPE on blazars with peak frequencies in the soft X-ray band or AGNs exhibiting thermal emission from their surrounding coronae at high redshifts would impose limits on the mixing term through a similar methodology, although its newly planned observations continue to prioritize sources at low redshifts. We note that planned missions such as the Enhanced X-ray Timing and Polarimetry mission (eXTP; [75]) and the X-ray Polarization Probe (XPP; [76]) with higher sensitivity will extend detection towards high-redshift sources within energy ranges of 0.5 – 30 keV and 0.2 – 60 keV, respectively. In addition, future polarimeters, such as the Compton Spectrometer and Imager (COSI; [77]) and the All-Sky Medium Energy Gamma-ray Observatory (AMEGO; [78]), targeting higher energy ranges (100 keV–5 MeV), are prepared to investigate the MeV polarization features, as shown in the lower panel of Fig. 6. These ongoing and planned missions will certainly provide a much larger sample for the investigation in this work and hopefully clear results would be obtained.

Acknowledgements

This work is supported by the National Natural Science Foundation of China under Nos. 11890692, 12133008, 12221003. We acknowledge the science research grant from the China Manned Space Project with No. CMS-CSST-2021-A04. We have utilized the following softwares: NumPy [79], Astropy [80–82], Matplotlib [83], gammaALPs [65], CIGALE [84–86], LePhare [87, 88].

-
- [1] B. Zhang, *The Physics of Gamma-Ray Bursts*, (2018)
 - [2] J. Jaeckel and A. Ringwald, *Annual Review of Nuclear and Particle Science* **60**, 405 (2010)
 - [3] Z. Cao *et al.*, *Science Advances* **9**, eadj2778 (2023)
 - [4] G. Galanti *et al.*, *Phys. Rev. Lett.* **131**, 251001 (2023)
 - [5] A. Mirizzi, G. G. Raffelt and P. D. Serpico, *Phys. Rev. D* **76**, 023001 (2007)
 - [6] M. A. Sanchez-Conde *et al.*, *Phys. Rev. D* **79**, 123511 (2009)
 - [7] A. Abramowski *et al.*, *Phys. Rev. D* **88**, 102003 (2013)
 - [8] M. Meyer, D. Montanino and J. Conrad, *J. Cosmol. Astropart. Phys.* **2014**, 003 (2014)
 - [9] Y. F. Liang *et al.*, *J. Cosmol. Astropart. Phys.* **2021**, 030 (2021)
 - [10] S. Jacobsen, T. Linden and K. Freese, *J. Cosmol. Astropart. Phys.* **2023**, 009 (2023)
 - [11] M. Kachelrieß and J. Tjemsland, *J. Cosmol. Astropart. Phys.* **2024**, 044 (2024)

- [12] F. Tavecchio, M. Roncadelli, G. Galanti and G. Bonnoli, *Phys. Rev. D* **86**, 085036 (2012)
- [13] M. Ajello *et al.*, *Phys. Rev. Lett.* **116**, 161101 (2016)
- [14] C. Zhang *et al.*, *Phys. Rev. D* **97**, 063009 (2018)
- [15] J. Zhou, Z. Wang, F. Huang and L. Chen, *J. Cosmol. Astropart. Phys.* **2021**, 007 (2021)
- [16] J. G. Cheng *et al.*, *Physics Letters B* **821**, 136611 (2021)
- [17] H. J. Li, X. J. Bi and P. F. Yin, *Chinese Physics C* **46**, 085105 (2022)
- [18] J. Davies, M. Meyer and G. Cotter, *Phys. Rev. D* **107**, 083027 (2023)
- [19] G. Galanti and M. Roncadelli, *Universe* **8**, 253 (2022)
- [20] C. Burrage, A. C. Davis and D. J. Shaw, *Phys. Rev. Lett.* **102**, 201101 (2009)
- [21] A. de Angelis, O. Mansutti, M. Persic and M. Roncadelli, *Mon. Not. Roy. Astron. Soc.* **394**, L21 (2009)
- [22] G. Galanti, M. Roncadelli, A. De Angelis and G. F. Big-nami, *Mon. Not. Roy. Astron. Soc.* **493**, 1553 (2020)
- [23] L. J. Dong, Y. G. Zheng and S. J. Kang, *Astrophys. J.* **952**, 152 (2023)
- [24] D. Hutsemékers and H. Lamy, *Astron. Astrophys.* **367**, 381 (2001)
- [25] P. Jain, S. Panda and S. Sarala, *Phys. Rev. D* **66**, 085007 (2002)
- [26] N. Agarwal, A. Kamal and P. Jain, *Phys. Rev. D* **83**, 065014 (2011)
- [27] A. Payez, J. R. Cudell and D. Hutsemékers, *J. Cosmol. Astropart. Phys.* **2012**, 041 (2012)
- [28] R. M. Yao, X. J. Bi, J. W. Wang and P. F. Yin, *Phys. Rev. D* **107**, 043031 (2023)
- [29] N. Agarwal, P. Jain, D. W. McKay and J. P. Ralston, *Phys. Rev. D* **78**, 085028 (2008)
- [30] P. Tiwari, *Phys. Rev. D* **86**, 115025 (2012)
- [31] G. Galanti, *Phys. Rev. D* **105**, 083022 (2022)
- [32] G. Galanti, M. Roncadelli, F. Tavecchio and E. Costa, *Phys. Rev. D* **107**, 103007 (2023)
- [33] G. Galanti, M. Roncadelli and F. Tavecchio, *Phys. Rev. D* **108**, 083017 (2023)
- [34] G. Galanti, *Phys. Rev. D* **107**, 043006 (2023)
- [35] A. Rubbia and A. Sakharov, *Astroparticle Physics* **29**, 20 (2008)
- [36] O. Mena, S. Razzaque and F. Villaescusa-Navarro, *J. Cosmol. Astropart. Phys.* **2011**, 030 (2011)
- [37] N. Bassan, A. Mirizzi and M. Roncadelli, *J. Cosmol. Astropart. Phys.* **2010**, 010 (2010)
- [38] E. Masaki, A. Aoki and J. Soda, *Phys. Rev. D* **96**, 043519 (2017)
- [39] P. Ubertini *et al.*, *Astron. Astrophys.* **411**, L131 (2003)
- [40] D. Yonetoku *et al.*, *Astrophys. J. Lett.* **743**, L30 (2011)
- [41] M. Kole *et al.*, *Astron. Astrophys.* **644**, A124 (2020)
- [42] T. Chattopadhyay *et al.*, *Astrophys. J.* **936**, 12 (2022)
- [43] S. McGlynn *et al.*, *Astron. Astrophys.* **499**, 465 (2009)
- [44] R. Gill, M. Kole and J. Granot, *Galaxies* **9**, 82 (2021)
- [45] D. Götz *et al.*, *Mon. Not. Roy. Astron. Soc.* **444**, 2776 (2014)
- [46] D. Götz *et al.*, *Mon. Not. Roy. Astron. Soc.* **431**, 3550 (2013)
- [47] R. Gupta *et al.*, *Mon. Not. Roy. Astron. Soc.* **511**, 1694 (2022)
- [48] R. Y. Guan and M. X. Lan, *Astron. Astrophys.* **670**, A160 (2023)
- [49] L. Li, S. S. Xue and Z. G. Dai, arXiv:2208.03583
- [50] M. Negro *et al.*, *Astrophys. J. Lett.* **946**, L21 (2023)
- [51] K. Toma *et al.*, *Astrophys. J.* **698**, 1042 (2009)
- [52] H. Ito *et al.*, *Astrophys. J.* **961**, 243 (2024)
- [53] D. Band *et al.*, *Astrophys. J.* **413**, 281 (1993)
- [54] T. Chattopadhyay *et al.*, *Astrophys. J.* **884**, 123 (2019)
- [55] L. Li and S. Shakeri, arXiv:2301.00576
- [56] A. K. Ganguly, *Introduction to Axion Photon Interaction in Particle Physics and Photon Dispersion in Magnetized Media*, (2012)
- [57] R. Durrer and A. Neronov, *The Astronomy and Astro-physics Review* **21**, 62 (2013)
- [58] A. Neronov and I. Vovk, *Science* **328**, 73 (2010)
- [59] F. Aharonian *et al.*, *Astrophys. J. Lett.* **950**, L16 (2023)
- [60] Y. Y. Huang *et al.*, *Astrophys. J. Lett.* **955**, L10 (2023)
- [61] J. Tjemsland, M. Meyer and F. Vazza, *Astrophys. J.* **963**, 135 (2024)
- [62] M. S. Pshirkov, P. G. Tinyakov and F. R. Urban, *Phys. Rev. Lett.* **116**, 191302 (2016)
- [63] M. Meyer, D. Horns and M. Raue, *Phys. Rev. D* **87**, 035027 (2013)
- [64] N. Jarosik *et al.*, *The Astrophysical Journal Supplement* **192**, 14 (2011)
- [65] M. Meyer, J. Davies and J. Kuhlmann, *PoS ICRC2021*, 557 (2021) arXiv:2108.02061
- [66] R. Jansson and G. R. Farrar, *Astrophys. J.* **757**, 14 (2012)
- [67] R. Jansson and G. R. Farrar, *Astrophys. J. Lett.* **761**, L11 (2012)
- [68] M. C. Beck *et al.*, *J. Cosmol. Astropart. Phys.* **2016**, 056 (2016)
- [69] V. Anastassopoulos *et al.*, *Nature Physics* **13**, 584 (2017)
- [70] A. Payez *et al.*, *J. Cosmol. Astropart. Phys.* **2015**, 006 (2015)
- [71] M. D. Marsh *et al.*, *J. Cosmol. Astropart. Phys.* **2017**, 036 (2017)
- [72] C. S. Reynolds *et al.*, *Astrophys. J.* **890**, 59 (2020)
- [73] J. Hulsman *et al.* [POLAR-2], *Proc. SPIE Int. Soc. Opt. Eng.* **11444**, 1-15 (2020)
- [74] M. L. McConnell *et al.*, *Proc. SPIE* **11821**, 118210P (2021) <https://doi.org/10.1117/12.2594737>
- [75] S. N. Zhang *et al.* [eXTP], *Proc. SPIE Int. Soc. Opt. Eng.* **9905**, 99051Q (2016)
- [76] K. Jahoda *et al.*, arXiv:1907.10190
- [77] J. Tomsick *et al.*, arXiv:1908.04334
- [78] J. McEnery *et al.*, *Bulletin of the AAS* **51**, 245 (2019) arXiv:1907.07558
- [79] C. R. Harris *et al.*, *Nature* **585**, 357 (2020)
- [80] Astropy Collaboration *et al.*, *Astron. Astrophys.* **558**, A33 (2013)
- [81] Astropy Collaboration *et al.*, *The Astronomical Journal* **156**, 123 (2018)
- [82] Astropy Collaboration *et al.*, *Astrophys. J.* **935**, 167 (2022)
- [83] J. D. Hunter, *Computing in Science & Engineering* **9**, 90 (2007)
- [84] M. Boquien *et al.*, *Astron. Astrophys.* **622**, A103 (2019)
- [85] G. Yang *et al.*, *Mon. Not. Roy. Astron. Soc.* **491**, 740 (2020)
- [86] G. Yang *et al.*, *Astrophys. J.* **927**, 192 (2022)
- [87] S. Arnouts *et al.*, *Mon. Not. Roy. Astron. Soc.* **310**, 540 (1999)
- [88] O. Ilbert *et al.*, *Astron. Astrophys.* **457**, 841 (2006)